

# Stiffness Copilot: An Impedance Policy for Contact-Rich Teleoperation

Yeping Wang<sup>1,2</sup>, Zhengtong Xu<sup>1,3</sup>, Pornthep Preechayasomboon<sup>1</sup>, Ben Abbatematteo<sup>1</sup>,  
Amirhossein H. Memar<sup>1</sup>, Nicholas Colonnese<sup>1</sup>, Sonny Chan<sup>1</sup>

stiffness-copilot.github.io

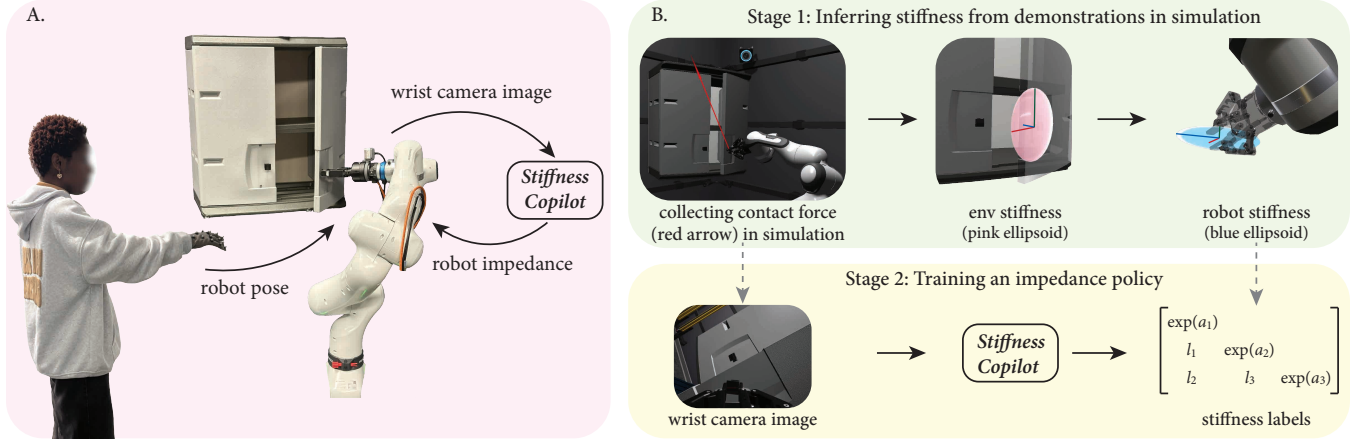


Fig. 1: We present Stiffness Copilot, a policy that adjusts the robot impedance for contact rich tasks. (A) Stiffness Copilot enables a shared-control teleoperation paradigm in which the human operator commands the robot pose while a vision-based policy adjusts the robot impedance. (B) To train Stiffness Copilot, we collect contact forces in simulation, from which we infer stiffness supervision. The policy is trained on simulated wrist-camera images and deployed zero-shot on real wrist-camera images.

**Abstract**—In teleoperation of contact-rich manipulation tasks, selecting robot impedance is critical but difficult. The robot must be compliant to avoid damaging the environment, but stiff to remain responsive and to apply force when needed. In this paper, we present Stiffness Copilot, a vision-based policy for shared-control teleoperation in which the operator commands robot pose and the policy adjusts robot impedance online. To train Stiffness Copilot, we first infer direction-dependent stiffness matrices in simulation using privileged contact information. We then use these matrices to supervise a lightweight vision policy that predicts robot stiffness from wrist-camera images and transfers zero-shot to real images at runtime. In a human-subject study, Stiffness Copilot achieved safety comparable to using a constant low stiffness while matching the efficiency of using a constant high stiffness.

## I. INTRODUCTION

Teleoperation has been widely used for remote manipulation in unstructured or safety-critical settings, and it is increasingly used to collect demonstration data for robot learning. To scale data collection, many systems rely on lightweight input devices such as VR controllers or a Space-Mouse, which are easy to deploy but typically provide limited or no force feedback, making contact-rich manipulation difficult because human operators cannot sense how the robot is loading the environment. In tasks such as door opening,

insertion, and wiping, small motion errors can produce large interaction forces, which may trigger protective stops and force operators to move slower than ideal.

Variable impedance can reduce this burden. The robot should remain compliant to tolerate command imprecision and avoid damaging contacts, yet become stiff when accurate motion and force transmission are needed. In practice, constant low stiffness improves safety but reduces responsiveness, while constant high stiffness improves efficiency but increases impact risk. This motivates our shared-control approach, where the operator commands pose and a vision-based policy adjusts robot impedance online to match the contact situation.

In this paper, we present Stiffness Copilot, a shared control method that automatically adjusts robot stiffness during teleoperation. The key challenge is that appropriate stiffness depends on the contact situation and task phase. Stiffness Copilot addresses this by learning to predict direction-dependent stiffness from wrist-camera images at runtime. We train the policy in two stages. First, in simulation we use privileged contact and simulator state information to infer stiffness labels for recurring interaction states across demonstrations. Second, we use these inferred stiffness matrices to supervise a lightweight vision policy, and use a vision foundation model with image augmentation to enable zero-shot sim-to-real transfer. The resulting policy outputs a symmetric positive definite stiffness matrix and runs in real time during teleoperation.

We conducted a human-subject experiment in which par-

<sup>1</sup>All authors are with Meta Reality Labs Research

<sup>2</sup>Yeping Wang is with University of Wisconsin-Madison, Madison, WI, USA [yeping@cs.wisc.edu](mailto:yeping@cs.wisc.edu)

<sup>3</sup>Zhengtong Xu is with Purdue University, West Lafayette, IN, USA

This work was conducted during internships at Meta Reality Labs.

ticipants performed tasks by teleoperating a robot with constant high stiffness, constant low stiffness, and with Stiffness Copilot. The results indicate that Stiffness Copilot combines the benefits of both baselines. It provides collision safety comparable to the low-stiffness setting while allowing operators to complete tasks as quickly as the high-stiffness setting. It largely avoids large impacts with the environment, yet still transmits sufficient force when needed. In addition, participants rated the robot with Stiffness Copilot as significantly more controllable, trustworthy, predictable, and fluent than both baselines.

The central contribution of this paper is Stiffness Copilot (§III), a vision-based impedance policy, and the shared-control paradigm it enables. We provide empirical evidence (§IV) that this paradigm improves task performance and user experience during teleoperation of contact-rich tasks.

## II. RELATED WORKS

Stiffness Copilot is a learning-based variable impedance policy for teleoperation. This section reviews three lines of work that inform our approach.

### A. Learning-Based Variable Impedance Policy

Contact-rich manipulation, such as surface wiping and peg-in-hole assembly, requires regulating interaction dynamics in addition to tracking motion, motivating impedance modulation during execution. Accordingly, many imitation learning methods augment pose prediction with an explicit compliance output. Works such as [1], [2], [3] train policies to output robot stiffness, regulating interaction via impedance control. In contrast, approaches like [4], [5], [6] predict desired forces, often utilizing admittance or hybrid force-position control schemes. Additionally, reinforcement learning methods [7] have adopted variable impedance control to autonomously discover compliance strategies for dynamic interaction tasks. However, these autonomous methods can not be directly used for shared control in teleoperation because the learned stiffness is optimized specifically for the policy’s own motion. Applying this trajectory-specific impedance to a human’s variable inputs inevitably results in suboptimal compliance or instability.

To generate stiffness labels in imitation learning, prior works primarily rely on two data collection modalities. The first is kinesthetic teaching [1], [2], where the operator physically guides the robot. This requires the robot to remain low-stiffness to accept human guidance. As the robot’s compliance damps the interaction forces, inferring precise stiffness parameters for rigid interactions from such softened signals often leads to conservative estimates [8]. The second approach is teleoperation with manual modulation [3], where operators adjust impedance by pressing a button. This restricts labels to pre-defined templates and fails to capture a mathematically precise full-matrix stiffness required for optimal interaction.

In contrast, our approach leverages privileged information from simulation to infer full stiffness matrix and distill it to a policy. Unlike real-world training which restricts exploration

to compliant regimes for safety, simulation permits safe learning of high-stiffness behaviors. Crucially, we utilize the explicit object state to computationally derive the physically optimal stiffness matrix from interaction dynamics. This transforms the problem into a supervised regression of precise, physics-grounded impedance targets, enabling the policy to learn complex, coupled stiffness behaviors impossible for humans to demonstrate manually.

### B. Variable Impedance in Teleoperation

Determining appropriate impedance parameters for teleoperation remains a challenge. Variable impedance control can be broadly categorized by how the stiffness is specified: explicitly by the human operator, implicitly via physiological signals, or automatically via task-based rules.

*Explicit Specification* – Prior works have developed interfaces that allow users to explicitly shape the stiffness ellipsoid using a tablet interface [9], a foot pedal [10], or interactive visualizations in Virtual Reality [11]. However, manually tuning a full stiffness matrix is cognitively demanding and often requires domain expertise. Recently, Hernandez *et al.* [12] introduced a haptic co-pilot that guides the operator to switch between discrete stiffness levels, simplifying the decision-making process.

*Implicit Estimation* – To achieve more natural modulation without manual input, the Tele-Impedance framework [13] estimates the human operator’s arm stiffness using electromyography and maps it to the robot. This allows the robot to mimic the human’s variable stiffness behaviors implicitly, though it requires additional physiological sensing hardware.

*Rule-Based Automation* – Alternatively, semi-autonomous methods reduce operator burden by regulating impedance using sensor feedback and task-specific heuristics. These methods typically adjust stiffness magnitude rather than orientation. A common pattern is to modulate only the stiffness magnitude, for example by increasing stiffness with measured external force to stabilize initial contact [14], adjusting stiffness from shear force to prevent object slip during grasping [15], or switching between a small number of impedance modes based on visually detected grasp phases [16]. While effective in their target settings, these rules are closely tied to specific sensing cues and hand-crafted phase definitions, which limits their flexibility.

*Learning-Based Estimation* – Unlike rule-based methods that rely on pre-defined heuristics for specific tasks, data-driven approaches infer appropriate impedance profiles from human demonstrations. Michel *et al.* [17], [18], [19] modulate stiffness inversely proportional to the trajectory variance in demonstrations and train Gaussian mixture models to infer stiffness based on sensed forces. However, this method is designed for tasks featuring continuous interaction with the environment, such as cutting. Moreover, it implicitly assumes that demonstrations use one strategy because they infer stiffness from trajectory variance. It remains unclear how to extend it to tasks with intermittent contact and multiple strategies.

### C. Learning-Based Assistance in Teleoperation

Shared control in teleoperation [20] is a collaborative control paradigm in which human commands and an assistive policy are blended in real time to drive the remote robot. Recent learning-based approaches first learn such a policy from data and then use it to assist teleoperation itself: for humanoid multi-contact manipulation, Rouxel et al. [21] learn a flow-matching policy from teleoperated demonstrations and deploy it in a shared-autonomy mode to provide automatic contact placement and stabilize the robot, while Yoneda et al. [22] and Sun et al. [23] train generative models that infer user intent and combine user inputs with expert-like actions for shared autonomy. In parallel, joint learning frameworks such as Human-Agent Joint Learning [24] and Incrementally Learned Shared Autonomy [25] explicitly close the loop between data collection and assistance: they start from weak or synthetic assistive policies, use them to support teleoperation and collect higher quality demonstrations, and gradually adapt the shared-control policy toward higher levels of autonomy while keeping the human in the loop.

## III. STIFFNESS COPILOT

In this section, we formalize the problem and describe the training and deployment of Stiffness Copilot.

### A. Problem Formulation

Stiffness Copilot predicts normalized stiffness profile  $\tilde{\mathbf{K}} \in \mathbb{R}^{3 \times 3}$ , which is a symmetric positive definite matrix with eigenvalues constrained to  $[0, 1]$ . At deployment time, we obtain the stiffness matrix  $\mathbf{K} \in \mathbb{R}^{3 \times 3}$  by linearly mapping these normalized eigenvalues from  $[0, 1]$  to a range  $[k_{\min}, k_{\max}]$  in N/m, and reconstructing a symmetric positive definite matrix with the same eigenvectors.

We choose to predict a normalized stiffness profile  $\tilde{\mathbf{K}}$  rather than a stiffness matrix in absolute units. In human-in-the-loop teleoperation, there is no single “correct” stiffness matrix. Different stiffness choices trade off tracking accuracy, responsiveness, safety, and operator comfort. The normalization allows the policy focus on directional stiffness allocation and the relative stiffness across directions. Moreover, absolute stiffness depends on the hardware and controller implementation. By predicting a normalized profile, we avoid tying the policy to a particular hardware, and adapt to a new robot by simply selecting appropriate  $k_{\min}$  and  $k_{\max}$  for that hardware.

### B. Demonstration in Simulation

We collect training demonstrations in a simulation-based teleoperation environment. In this simulation, we randomize object placements at the beginning of each episode. For the  $n$ -th demonstration, we record a time series  $\{\mathbf{I}_{n,t}, \mathbf{R}_{n,t}, \mathbf{f}_{n,t}, \mathbf{s}_{n,t}\}_t$  at 10 Hz, where  $\mathbf{I}_{n,t}$  is the RGB image from the wrist-mounted camera,  $\mathbf{R}_{n,t} \in \text{SO}(3)$  is the orientation of the wrist camera in the environment frame,  $\mathbf{f}_{n,t} \in \mathbb{R}^3$  is the net contact force between the robot and the environment, and  $\mathbf{s}_{n,t}$  encodes task-specific environment state. For example,  $s$  represents the door opening angle in

a door-opening task. In a vase-wiping task,  $s$  represents the sponge pose relative to the vase.

### C. Inference of Environment Stiffness

This section is to compute environment stiffness matrix for each environment state  $\mathbf{K}_e(\mathbf{s}_{n,t})$ . We first normalize each dimension of the environment state  $\mathbf{s}$  to have zero mean and unit variance over the dataset. For each environment state  $\mathbf{s}_{n,t}$ , we define a local neighborhood  $\mathcal{N}(\mathbf{s}_{n,t})$  as the set of  $k$  nearest neighbors of  $\mathbf{s}_{n,t}$  under the Euclidean distance in this normalized space, where  $k$  is chosen larger than the dimension of the task space so that a full stiffness matrix can be estimated. We denote the corresponding set of contact forces by  $\mathcal{F}(\mathbf{s}_{n,t}) = \{\mathbf{f}_{n',t'} \mid \mathbf{s}_{n',t'} \in \mathcal{N}(\mathbf{s}_{n,t})\}$ . Note that although  $\mathbf{f}$  involves forces caused by friction and gravity, because we are using a high-stiffness robot in simulation, contact forces dominate the signal.

Prior work [26] infers stiffness from the covariance of the contact forces,  $\mathbf{K}_e^2 \propto \mathbb{E}_{\mathbf{f} \in \mathcal{F}(\mathbf{s}_{n,t})}[\mathbf{f} \mathbf{f}^\top]$ . However, this approach depends on how contact directions are sampled. Frequently sampled directions contribute more to the covariance and bias the results. Moreover, symmetric positive definite matrices form a curved Riemannian manifold rather than a Euclidean space, Euclidean operations such as element-wise averaging can be geometrically inconsistent and produce the swelling effect, a non-physical increase in determinant that can cause numerical chattering and “ghost” stiffness in unobserved directions [27].

Instead, we partition the unit sphere into  $m$  fixed angular sectors (e.g., using a regular grid in spherical coordinates) and aggregate forces within each sector. For the  $i$ -th sector, we collect all forces whose direction falls into this sector. If the sector contains at least one sample, we define a representative force  $\tilde{\mathbf{f}}_i$  by aligning it with the average direction in the sector and assigning it the 95th percentile magnitude observed in that sector. This yields a sector-wise outer product  $\tilde{\mathbf{f}}_i \tilde{\mathbf{f}}_i^\top + \varepsilon \mathbf{I}$ , where  $\varepsilon \mathbf{I}$  is a small isotropic regularizer that ensures the matrix is full rank. To combine sector information, we compute a log-Euclidean mean [27]. We first apply the matrix logarithm to map each matrix to a flat vector space, take the arithmetic mean in that log domain, and then apply the matrix exponential to map back to the symmetric positive definite manifold. Concretely,

$$\mathbf{S}_e(\mathbf{s}_{n,t}) = \frac{1}{m_{\text{valid}}} \sum_{i=1}^{m_{\text{valid}}} \log(\tilde{\mathbf{f}}_i \tilde{\mathbf{f}}_i^\top + \varepsilon \mathbf{I}), \quad (1)$$

$$\mathbf{K}_e(\mathbf{s}_{n,t}) \propto \exp\left(\frac{1}{2} \mathbf{S}_e(\mathbf{s}_{n,t})\right), \quad (2)$$

where  $m_{\text{valid}}$  is the number of non-empty sectors.

### D. Computation of Robot Stiffness

After inferring environment stiffness  $\mathbf{K}_e(\mathbf{s}_{n,t})$ , we construct the robot stiffness by making it complementary to the environment, that is, soft along directions where the environment is stiff and vice versa.

First, we perform eigendecomposition on the force matrix computed in the previous section, such that  $\mathbf{K}_e = \mathbf{Q}_e \mathbf{\Lambda}_M \mathbf{Q}_e^\top$ ,

where  $\mathbf{Q}_e \in \text{SO}(3)$  represents the principal directions of the environment stiffness in the world frame, and the environment stiffness eigenvalues are  $\Lambda_e = \Lambda_M^{1/2}$ . To encode that the robot should be soft where the environment is stiff, we keep the same eigenvectors and apply a monotonically decreasing mapping  $h(\cdot)$  to the eigenvalues. A simple choice is  $h(\lambda_e^j) = 1/(\lambda_e^j + \varepsilon)$ , where  $\lambda_e^j$  is the diagonal element of  $\Lambda_e$  and  $\varepsilon$  is a small number. We then normalize the resulting values over the dataset to target range  $[0, 1]$ . The normalized robot eigenvalues  $\tilde{\kappa}^j$  are computed as:

$$\kappa^j = h(\lambda_e^j), \quad \tilde{\kappa}^j = \text{clamp}\left(\frac{\kappa^j - \kappa_{\min}}{\kappa_{\max} - \kappa_{\min}}, 0, 1\right), \quad (3)$$

where  $\kappa_{\min}$  and  $\kappa_{\max}$  are global lower and upper percentiles of the dataset. We construct the normalized eigenvalue matrix  $\tilde{\Lambda}_r = \text{diag}(\tilde{\kappa}^1, \tilde{\kappa}^2, \tilde{\kappa}^3)$ .

The trained policy will predict robot stiffness in the wrist camera frame. We obtain the camera-frame eigenvectors by rotating the world-frame eigenvectors  $\mathbf{Q}_e$  by the camera orientation  $\mathbf{R}_{n,t}$  as  $\mathbf{Q}_r = \mathbf{R}_{n,t}^\top \mathbf{Q}_e$ . We then construct the normalized stiffness label  $\tilde{\mathbf{K}}_r(\mathbf{s}_{n,t}) = \mathbf{Q}_{\text{cam}} \tilde{\Lambda}_r \mathbf{Q}_{\text{cam}}^\top$ . By construction,  $\tilde{\mathbf{K}}_r$  is symmetric positive definite with eigenvalues bounded in  $[0, 1]$ , serving as a label for policy learning.

### E. Training Dataset

From the procedure above we obtain training pairs  $\{(\mathbf{I}_{n,t}, \tilde{\mathbf{K}}_r(\mathbf{s}_{n,t}))\}$ . A valid stiffness matrix must be symmetric positive definite. Following prior work [28], [29], [3], we encode  $\tilde{\mathbf{K}}_r$  using its Cholesky factorization,  $\tilde{\mathbf{K}}_r = \mathbf{L}\mathbf{L}^\top$ , where  $\mathbf{L}$  is a lower-triangular matrix with strictly positive diagonal entries.

In addition, we parametrize the diagonal entries of  $\mathbf{L}$  in log-space, so that the policy predicts unconstrained diagonal parameters. The exponential mapping guarantees a smooth one-to-one correspondence between the network outputs and symmetric positive definite stiffness matrices.

$$\mathbf{L} = \begin{bmatrix} \exp(a_1) & 0 & 0 \\ l_{21} & \exp(a_2) & 0 \\ l_{31} & l_{32} & \exp(a_3) \end{bmatrix}, \quad (4)$$

where  $a_1, a_2, a_3, l_{21}, l_{31}$ , and  $l_{32}$  are the output of a policy.

### F. Policy Training

We train a policy that maps a single RGB image from the wrist-mounted camera to a normalized stiffness profile in the camera frame. The input to the network is the image  $\mathbf{I}_{n,t}$ , and the output is a set of unconstrained parameters that define the Cholesky factor  $\mathbf{L}$  of the normalized stiffness matrix  $\tilde{\mathbf{K}}_r$ .

The visual backbone is based on the small variant of DINOv3 [30]. We use the CLS token to extract a feature vector from the input image. The backbone weights are frozen during training. The extracted visual features are passed to a feedforward network consisting of 2 fully connected layers with 256 activations. The final layer outputs the 6 scalar values in Eq. 4. We train the network using a supervised regression loss between the predicted stiffness matrix and the target label obtained from demonstrations. Specifically,

given a predicted Cholesky factor  $\hat{\mathbf{L}}$  and ground-truth factor  $\mathbf{L}$ , we minimize MSE loss on Cholesky parameters.

To improve generalization and sim-to-real transfer, we apply image augmentations during training, including random cropping, color and brightness jitter, and Gaussian noise. We pool demonstrations from all tasks into a single dataset and train one policy jointly across the three evaluation tasks.

### G. Deployment

We run policy inference at 90 Hz. At each step, the policy outputs a normalized stiffness profile  $\tilde{\mathbf{K}}_t$ . We scale its eigenvalues from  $[0, 1]$  to  $[k_{\min}, k_{\max}]$  in N/m to obtain  $\mathbf{K}_t^{\text{raw}}$ , and then smooth  $\mathbf{K}_t^{\text{raw}}$  on the symmetric positive definite manifold using a log-domain exponential moving average. At each step,  $\mathbf{K}_t = \exp((1 - \alpha) \log(\mathbf{K}_{t-1} + \varepsilon \mathbf{I}) + \alpha \log(\mathbf{K}_t^{\text{raw}} + \varepsilon \mathbf{I}))$ , where  $\log(\cdot)$  and  $\exp(\cdot)$  denote the matrix logarithm and exponential. We set  $\alpha = 0.2$ .

## IV. EVALUATION

Our evaluation focused on assessing how Stiffness Copilot may influence teleoperation in contact-rich tasks. Our central hypothesis is that a robot with Stiffness Copilot will lead to better task performance and user perception than robots with constant stiffness.

### A. Experimental Design & Conditions

Our user evaluation followed a within-participants design, with each participant working with the robot under all conditions. We counterbalanced the order in which the conditions were presented.

*Low Impedance* (Baseline 1): We configure the robot with a uniformly compliant impedance profile: translational stiffness is fixed at 300 N/m along all axes, with translational damping set to 20 N·s/m. For orientation control, the rotational stiffness and damping are set to 10 N·m/rad and 3.0 N·m·s/rad, respectively.

*High Impedance* (Baseline 2): The high-impedance baseline maintains a rigid behavior throughout the task, with translational stiffness set to 3000 N/m in all directions and translational damping increased to 70 N·s/m. The rotational stiffness and damping are set to 100 N·m/rad and 8.0 N·m·s/rad, respectively.

*Variable Impedance with Stiffness Copilot* (ours): We use the Stiffness Copilot proposed in this paper to set the robot translational stiffness. Specifically, we linearly scale the eigenvalues of the policy output matrix to lie between 300 and 3000 N/m. Translational damping is computed in the same eigenspace as  $d = 1.4\sqrt{k}$ , where  $k$  is the corresponding stiffness eigenvalue (N/m) and  $d$  is the resulting damping eigenvalue (N·s/m). We use a constant medium setting with rotational stiffness and damping fixed at 40 N·m/rad and 5.5 N·m·s/rad, respectively.

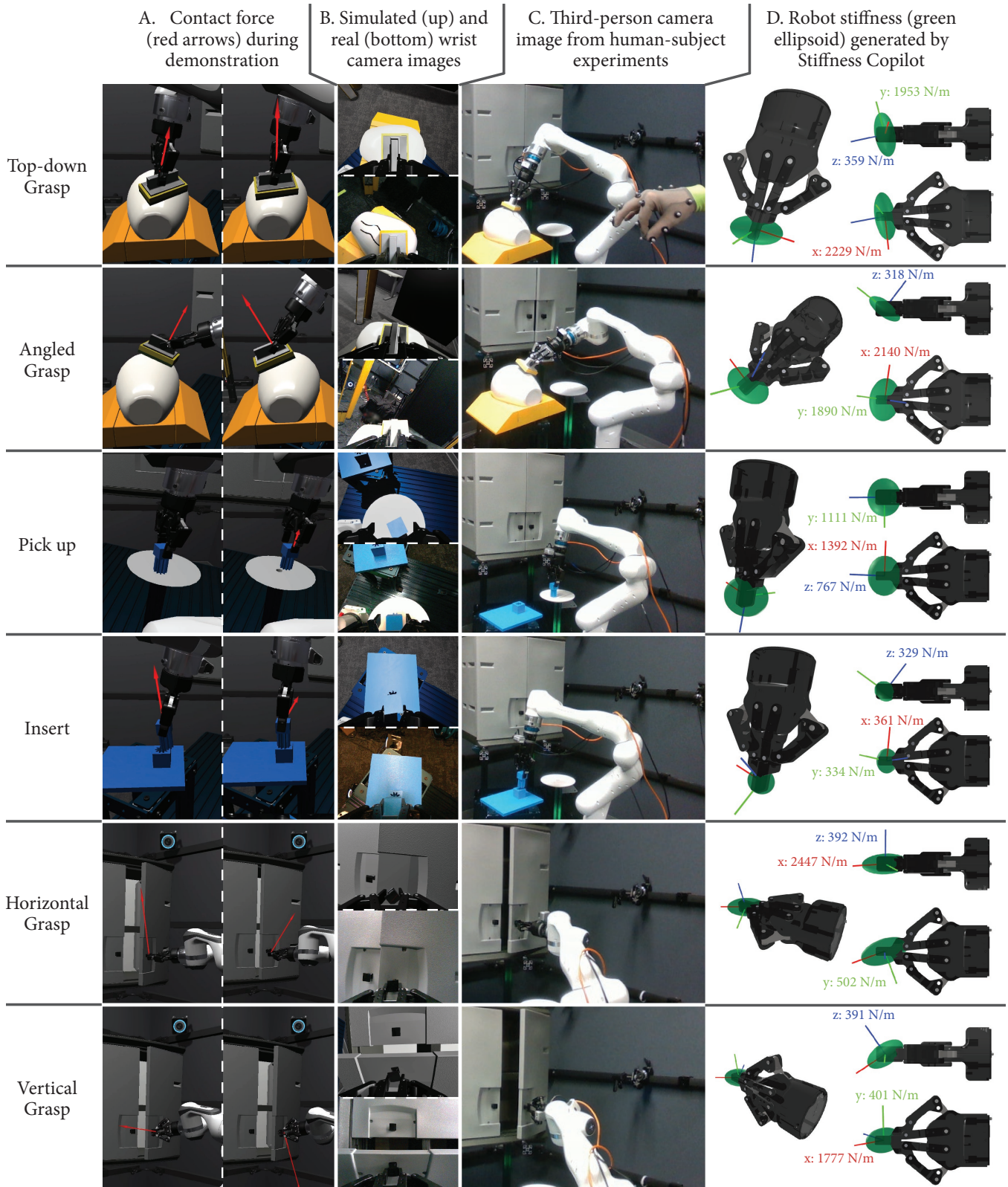


Fig. 2: Overview of Stiffness Copilot execution in the human-subjective experiment. Each row shows a representative situation. (A) We first collected contact forces in simulation to infer robot stiffness, which provided training data for Stiffness Copilot. (B) Stiffness Copilot was trained using simulated wrist-camera images (upper) and was deployed using real wrist-camera images (lower) during policy rollout, illustrating the sim-to-real gap. (C) Third-person views from our user study, where a participant teleoperated the robot. (D) Stiffness produced by Stiffness Copilot is visualized as a green ellipsoid, where a longer ellipsoid axis indicates larger translation stiffness in that direction. We also annotate the stiffness magnitude along each axis. In Vase Wiping (top two rows), despite different grasp poses, the robot remained compliant perpendicular to the contact surface and stiff in other directions. In Peg-in-Hole (middle two rows), the robot was stiff while picking up the block and compliant during peg insertion. In Door Opening (bottom two rows), despite different grasp poses, the robot was stiff along the opening direction and compliant in other directions.

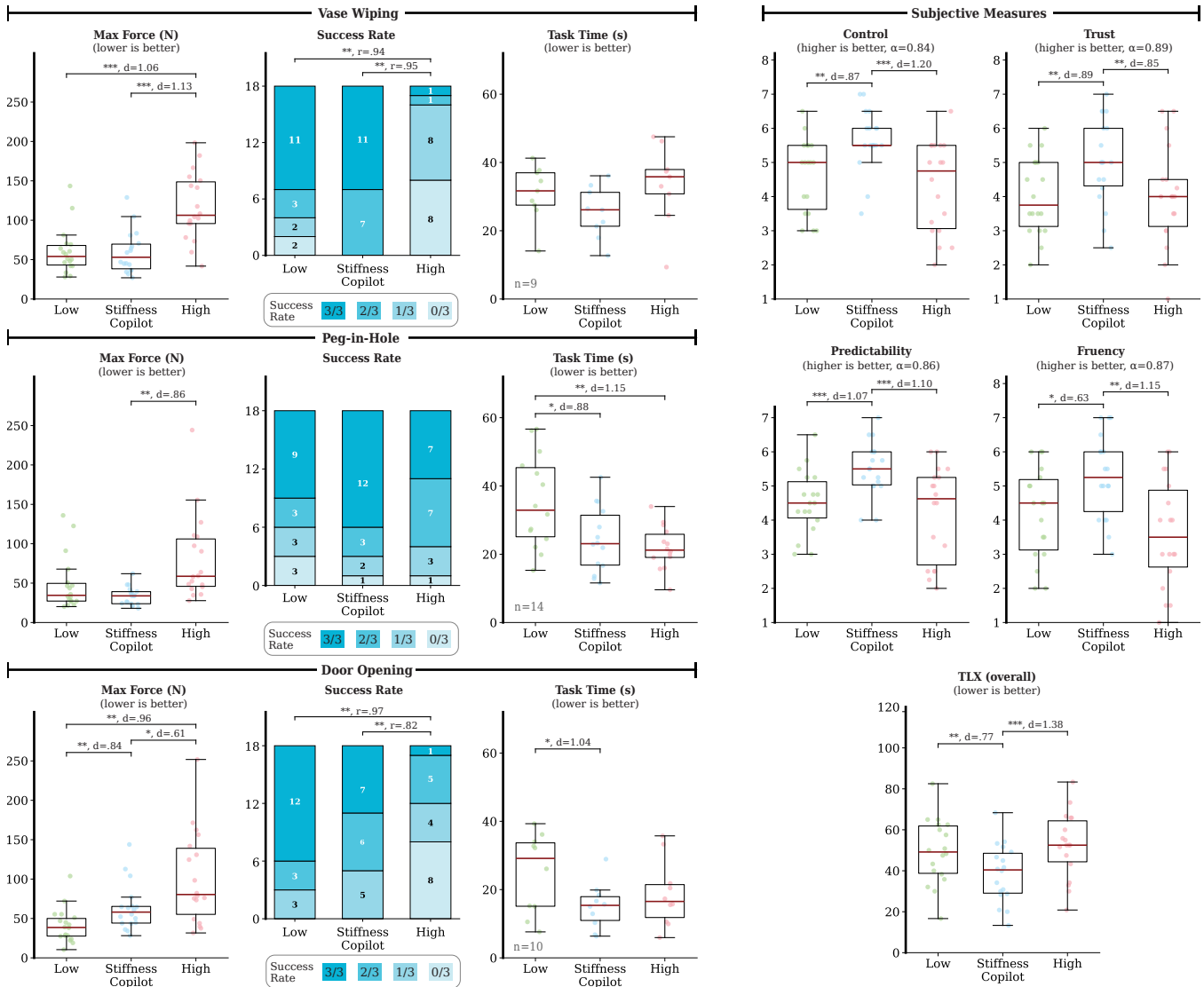


Fig. 3: Visualization of our study results. For box and whisker plots, the top and bottom of each box represent the first and third quartiles, and the line inside each box is the statistical median of the data. The length of the box is defined as the interquartile range (IQR). The whiskers are within a maximum of 1.5 IQR. \*/ \*\*/\*\*\* indicate significance levels  $p < .05/.01/.001$ .  $d$  is Cohen’s  $d$  for paired  $t$ -tests and  $r$  is the Wilcoxon effect size.

## B. Experimental Tasks

Our experiment involves teleoperating the robot to complete 3 contact-rich tasks (Figure 2):

**Vase Wiping:** Participants teleoperated the robot to grasp a sponge and wipe the marker trace from the vase. This task requires sufficient contact force to remove the trace without triggering the robot’s protective stop.

**Peg-in-Hole:** Participants picked up a 10-tooth gear shape pin and insert it into a same-shaped hole with 0.3 mm clearance.

**Cabinet Door Opening:** Participants opened a cabinet door to 90° using only the handle. This task requires moving the end-effector along the door’s opening arc, which is difficult without force feedback; deviations from the arc can produce large interaction forces with the environment.

## C. Implementation Details

We track the operator hand pose with an OptiTrack motion-capture system at 120 Hz. The tracked 6D hand pose

is mapped to commands for a Franka Research 3 (FR3) arm using RelaxedIK [31], [32] and executed with the Deoxys operational-space impedance controller [33]. We use a foot pedal as a clutch to enable or pause control.

To compute stiffness labels, one author provided 16 demonstrations per task in simulation. The simulator is built in Unreal Engine [34] with a customized physics solver that uses reduced-order models with data-driven hyper-reduction to simulate contact among rigid and compliant objects at interactive rates [35], [36], [37], providing rich per-contact state for dexterous manipulation. A Meta Quest 3 was used as the VR display during simulated teleoperation.

In the human-subject experiment, we use a RealSense D405 as the wrist camera. The camera resolution is 640×480 at 90 Hz. To measure contact forces, we use a Bota Systems SensONE Gen-A force-torque sensor sampled at 1000 Hz. Policy rollouts at 90 Hz on a NVIDIA GeForce 5080 GPU.

TABLE I  
SUMMARY OF USER STUDY RESULTS ACROSS STIFFNESS CONDITIONS. BEST VALUES ARE SHOWN IN **BOLD**.

	Metric	Low Stiffness Mean (SD)	Stiffness Copilot Mean (SD)	High Stiffness Mean (SD)	Statistical Test	
Objective Measures	Vase Wiping	Max Force (N)	60.58 (29.23)	<b>59.28</b> (27.04)	117.46 (42.87)	$F(2, 34) = 17.15, p < .001^{***}, \eta_p^2 = 0.502$
		Success Rate	0.76 (0.36)	<b>0.87</b> (0.17)	0.24 (0.28)	$\chi^2 = 20.13, p < .001^{***}, W = 0.559$
		Time (s)	30.96 (8.12)	<b>25.31</b> (7.54)	33.62 (11.57)	$F(2, 16) = 4.29, p < .05^*, \eta_p^2 = 0.349$
	Peg-in-Hole	Max Force (N)	49.00 (34.25)	<b>33.41</b> (11.67)	80.60 (54.44)	$F(2, 34) = 6.99, p < .01^{**}, \eta_p^2 = 0.291$
		Success Rate	0.67 (0.40)	<b>0.81</b> (0.31)	0.70 (0.30)	$\chi^2 = 3.21, p = 0.201, W = 0.089$
		Time (s)	35.35 (13.59)	24.22 (9.58)	<b>21.95</b> (6.31)	$F(2, 26) = 12.01, p < .001^{***}, \eta_p^2 = 0.480$
	Door Opening	Max Force (N)	<b>40.96</b> (21.97)	63.63 (29.82)	101.42 (58.96)	$F(2, 34) = 11.89, p < .001^{***}, \eta_p^2 = 0.412$
		Success Rate	<b>0.83</b> (0.26)	0.70 (0.28)	0.31 (0.33)	$\chi^2 = 19.77, p < .001^{***}, W = 0.549$
		Time (s)	24.89 (11.68)	<b>15.09</b> (6.67)	18.63 (9.67)	$F(2, 18) = 4.99, p < .05^*, \eta_p^2 = 0.357$
Subjective Measures	Control	4.64 (1.10)	<b>5.67</b> (0.89)	4.29 (1.34)	$F(2, 34) = 10.16, p < .001^{***}, \eta_p^2 = 0.374$	
	Trust	4.03 (1.14)	<b>5.01</b> (1.27)	4.01 (1.48)	$F(2, 34) = 7.22, p < .01^{**}, \eta_p^2 = 0.298$	
	Predictability	4.51 (0.94)	<b>5.51</b> (0.79)	4.21 (1.38)	$F(2, 34) = 11.31, p < .001^{***}, \eta_p^2 = 0.400$	
	Fluency	4.21 (1.34)	<b>5.28</b> (1.23)	3.61 (1.59)	$F(2, 34) = 8.44, p < .01^{**}, \eta_p^2 = 0.332$	
	NASA-TLX	49.33 (15.89)	<b>38.73</b> (14.15)	52.43 (16.00)	$F(2, 34) = 11.36, p < .001^{***}, \eta_p^2 = 0.401$	

#### D. Experimental Procedure

After providing consent, participants were introduced to the study goal and teleoperation interface. For each condition, they first completed a pick-and-place practice task, then performed three trials of each task in a fixed order: vase wiping, peg-in-hole, and cabinet opening. Each trial had a strict 60 s time limit. Upon finishing all nine trials (3 tasks  $\times$  3 trials) for a specific condition, participants completed subjective questionnaires about their experience in the condition. This procedure, including performing the practice and experimental tasks and filling out the questionnaire, was repeated for other conditions. After finishing all conditions, participants completed a demographic questionnaire and a semi-structured interview. Participants received 25 USD for approximately 60 minutes.

#### E. Measures

We used both objective and subjective measures to evaluate task performance and user experience. For the objective measures, we recorded the peak contact force from the wrist force-torque sensor in each trial, then averaged it across trials. We also calculated task success rates: a trial was marked as failed if the emergency stop was triggered or if it exceeded the 60 s time limit. For trials that succeeded, we further measured task completion time for successful trials and report the average across trials. If a participant failed all three trials of a given task, we excluded that participant from the completion-time analysis for that task.

For subjective measures, we used the same questionnaire from prior teleoperation work [38], [39] to measure perceived control, predictability, fluency, and trust in the robot system. We used NASA TLX [40] to measure perceived workload.

#### F. Participants

We recruited 18 participants from a tech company campus (7 females and 11 males), aged from 23 to 47 ( $M=31.28$ ,  $SD=5.44$ ). 12 participants reported prior teleoperation experience. Participants reported moderate-to-high familiarity with robots ( $M=4.64$ ,  $SD=2.04$ ) and 3D video games ( $M=5.17$ ,  $SD=2.09$ ) on a 7-point Likert scale. Most participants were right-handed (15 right-handed, 3 left-handed), and all participants operated the robot with their right hand.

#### G. Results

Figure 3 and Table I summarize our results. We analyzed continuous measures using a one-way repeated-measures ANOVA, followed by Holm-corrected paired t-tests for post hoc pairwise comparisons. Success rate is a discrete measure and was analyzed using Friedman test followed by Holm-corrected Wilcoxon signed-rank tests.

*Task Performance* – Our results indicate that Stiffness Copilot consistently led to smaller contact force compared to the high stiffness condition across all three manipulation tasks (all  $p < .05$  and Cohen’s  $d > .6$ ). In addition, Stiffness Copilot achieved higher success rates than the high-stiffness condition across tasks, with significant differences for Vase Wiping and Door Opening ( $p < .01$  for both) but not for Peg-in-Hole insertion. One possible explanation is that peg-in-hole insertion is more perception-limited, requiring precise visual alignment before insertion. This perceptual bottleneck may dominate performance and reduce the observable impact of robot impedance. Compared to the low stiffness robot, Stiffness Copilot reduced task time across all tasks, with significant reductions for Peg-in-Hole and Cabinet Opening (both  $p < .05$  and  $d > .8$ ), but not for Vase Wiping ( $p = .091$  and  $d = .72$ ). We attribute the non-significant result to reduced statistical power, as only  $n=9$  participants were included in the time analysis for that task after excluding participants who failed all three trials (more details in §IV-E).

*User Perception* – Our results revealed that participants perceived the robot with Stiffness Copilot to be significantly more under control, predictable, fluent, and trustworthy, and have significantly lower workload (all  $p < .05$ ) with medium-to-large effect sizes (all  $d > .6$ ), compared to both the high stiffness and low stiffness robot.

In the post-experiment interview, participants often described the low-stiffness robot as slow, flowy, or delayed. They also expressed the difficulty in high stiffness condition, for example, P4 commented that “*On the [high-stiffness] condition, I was trying a lot harder to try to follow the path of the cabinet door better to open it up. For the [Stiffness Copilot] condition, I didn’t need to think about this.*” Meanwhile, P1 commented that “*[Stiffness Copilot] was as responsive as the [High Stiffness] condition, but it*

*felt more in control.*” Also, P2 commented that “*With the [Stiffness Copilot] condition, it seems like the whole arm sort of like knew what I am supposed to do... so I can do it naturally and the arm will follow.*”

*Summary* – The results indicate that Stiffness Copilot combines the benefits of both baselines. It provides collision safety, reflected by lower contact forces, comparable to the low-stiffness setting while allowing operators to complete tasks as quickly as the high-stiffness setting. Participants also rated Stiffness Copilot as significantly more controllable, trustworthy, predictable, and fluent than either baseline.

## V. DISCUSSION

In this work, we proposed Stiffness Copilot, a vision-based policy that takes wrist-camera images as input and outputs direction-dependent translational stiffness matrix. Stiffness Copilot enables a shared-control teleoperation paradigm in which the operator commands target poses while the policy modulates robot stiffness online. In a user study, Stiffness Copilot matched the collision safety of a low-stiffness baseline and the task efficiency of a high-stiffness baseline, while improving user experience.

While our results show the effectiveness of Stiffness Copilot, several limitations motivate future work. First, we only modulate translational impedance and keep rotational impedance fixed; extending the policy to jointly adapt rotational stiffness and damping is an important next step. Second, our current supervision and training data focus on quasi-static contact interactions. Future work should extend Stiffness Copilot to more dynamic regimes, such as hammering, where high stiffness supports fast and accurate swings, while lowering stiffness at impact reduce impact transmission to the arm. Third, although we evaluate Stiffness Copilot in a shared-control setting, the same mechanism could be integrated into autonomous manipulation policies to adapt impedance during execution. Finally, while we use a single policy across three tasks, we do not evaluate generalization to unseen objects or tasks, such as opening a previously unseen door. Scaling to broader settings may require more diverse training data and more expressive architectures, enabling a single policy to adjust impedance across a wider range of contact-rich tasks.

## REFERENCES

- [1] M. Aburub, C. C. Beltran-Hernandez, T. Kamijo, and M. Hamaya, “Learning diffusion policies from demonstrations for compliant contact-rich manipulation,” *arXiv preprint arXiv:2410.19235*, 2024.
- [2] Y. Hou, Z. Liu, C. Chi, E. Cousineau, N. Kuppusswamy, S. Feng, B. Burchfiel, and S. Song, “Adaptive compliance policy: Learning approximate compliance for diffusion guided control,” in *2025 IEEE Int. Conf. Robotics Automation (ICRA)*. IEEE, 2025, pp. 4829–4836.
- [3] T. Kamijo, C. C. Beltran-Hernandez *et al.*, “Learning variable compliance control from a few demonstrations for bimanual robot with haptic feedback teleoperation system,” in *2024 IEEE/RSJ Int. Conf. Intelligent Robots Systems (IROS)*. IEEE, 2024, pp. 12 663–12 670.
- [4] P. Kormushev, S. Calinon, and D. G. Caldwell, “Imitation learning of positional and force skills demonstrated via kinesthetic teaching and haptic input,” *Advanced Robotics*, vol. 25, no. 5, pp. 581–603, 2011.
- [5] B. Zhou, R. Jiao, Y. Li, X. Yuan, F. Fang, and S. Li, “Admittance visuomotor policy learning for general-purpose contact-rich manipulations,” *IEEE Transactions on Industrial Electronics*, 2025.
- [6] Y. Wu, Z. Chen, F. Wu, L. Chen, L. Zhang, Z. Bing, A. Swikir, S. Hadadin, and A. Knoll, “Tacdiffusion: Force-domain diffusion policy for precise tactile manipulation,” *arXiv preprint arXiv:2409.11047*, 2024.
- [7] R. Martín-Martín, M. A. Lee, R. Gardner, S. Savarese *et al.*, “Variable impedance control in end-effector space: An action space for reinforcement learning in contact-rich tasks,” in *2019 IEEE/RSJ Int. Conf. Intelligent Robots Systems (IROS)*. IEEE, 2019, pp. 1010–1017.
- [8] N. Hogan and S. P. Buerger, “Impedance and interaction control,” in *Robotics and automation handbook*. CRC press, 2018, pp. 375–398.
- [9] L. Peternel, N. Beckers, and D. A. Abbink, “Independently commanding size, shape and orientation of robot endpoint stiffness in teleimpedance by virtual ellipsoid interface,” in *2021 20th International Conference on Advanced Robotics (ICAR)*. IEEE, 2021, pp. 99–106.
- [10] S. Klevering, W. Muge, D. A. Abbink, and L. Peternel, “Foot-operated tele-impedance interface for robot manipulation tasks in interaction with unpredictable environments,” in *2022 IEEE/RSJ Int. Conf. Intelligent Robots Systems (IROS)*. IEEE, 2022, pp. 3497–3504.
- [11] A. D. Rosales, J. Rodriguez-Nogueira, E. Matheson *et al.*, “Interactive multi-stiffness mixed reality interface: Controlling and visualizing robot and environment stiffness,” in *2024 IEEE/RSJ Int. Conf. Intelligent Robots Systems (IROS)*. IEEE, 2024, pp. 13 479–13 486.
- [12] P. G. Hernandez, J. M. Jakobsen, C. Pacchierotti, F. Chinello, and C. Fang, “Stiffness regulation co-pilot in bilateral teleimpedance control: a preliminary user study,” in *Proc. IEEE Int. Conf. Robotics Automation (ICRA)*, 2025.
- [13] A. Ajoudani, N. Tsagarakis, and A. Bicchi, “Tele-impedance: Teleoperation with impedance regulation using a body-machine interface,” *Int. J. Robotics Research*, vol. 31, no. 13, pp. 1642–1656, 2012.
- [14] L. Muratore, A. Laurenzi, E. M. Hoffman, L. Baccelliere, N. Kashiri, D. G. Caldwell, and N. G. Tsagarakis, “Enhanced tele-interaction in unknown environments using semi-autonomous motion and impedance regulation principles,” in *2018 IEEE International Conference on Robotics and Automation (ICRA)*. IEEE, 2018, pp. 5813–5820.
- [15] M. Popken, J. M. Prendergast, M. Wiertelowski, and L. Peternel, “An adaptive semi-autonomous impedance controller for teleoperated object grasping based on human grip safety margin,” in *IEEE-RAS Int. Conf. Humanoid Robots (Humanoids)*. IEEE, 2023, pp. 1–8.
- [16] Y.-C. Huang, D. A. Abbink, and L. Peternel, “A semi-autonomous tele-impedance method based on vision and voice interfaces,” in *2021 Int. Conf. Advanced Robotics (ICAR)*. IEEE, 2021, pp. 180–186.
- [17] Y. Michel, R. Rahal, C. Pacchierotti, P. R. Giordano *et al.*, “Bilateral teleoperation with adaptive impedance control for contact tasks,” *IEEE Robotics and Automation Letters*, vol. 6, no. 3, pp. 5429–5436, 2021.
- [18] Y. Michel, Z. Li, and D. Lee, “A learning-based shared control approach for contact tasks,” *IEEE Robotics and Automation Letters*, vol. 8, no. 12, pp. 8002–8009, 2023.
- [19] Y. Michel, Y. Abdelhalem, and G. Cheng, “Passivity-based teleoperation with variable rotational impedance control,” *IEEE Robotics and Automation Letters*, 2024.
- [20] G. Li, Q. Li, C. Yang, Y. Su, Z. Yuan, and X. Wu, “The classification and new trends of shared control strategies in telerobotic systems: A survey,” *IEEE Trans. Haptics*, vol. 16, no. 2, pp. 118–133, 2023.
- [21] Q. Rouxel, A. Ferrari, S. Ivaldi, and J.-B. Mouret, “Flow matching imitation learning for multi-support manipulation,” in *2024 IEEE-RAS 23rd International Conference on Humanoid Robots (Humanoids)*. IEEE, 2024, pp. 528–535.
- [22] T. Yoneda, L. Sun, B. Stadie *et al.*, “To the noise and back: Diffusion for shared autonomy,” *arXiv preprint arXiv:2302.12244*, 2023.
- [23] L. Sun, J. Ji, X. Tan, and M. R. Walter, “Flashback: Consistency model-accelerated shared autonomy,” *arXiv preprint arXiv:2505.16892*, 2025.
- [24] S. Luo, Q. Peng, J. Lv, K. Hong, K. R. Driggs-Campbell, C. Lu, and Y.-L. Li, “Human-agent joint learning for efficient robot manipulation skill acquisition,” *arXiv preprint arXiv:2407.00299*, 2024.
- [25] Y. Tao, G. Qiao, D. Ding, and Z. Erickson, “Incremental learning for robot shared autonomy,” *arXiv preprint arXiv:2410.06315*, 2024.
- [26] J. Duan, Y. Ou, S. Xu, Z. Wang, A. Peng, X. Wu, and W. Feng, “Learning compliant manipulation tasks from force demonstrations,” in *2018 IEEE Int. Conf. Cyborg and Bionic Systems (CBS)*. IEEE, 2018, pp. 449–454.
- [27] V. Arsigny, P. Fillard, X. Pennec, and N. Ayache, “Geometric means in a novel vector space structure on symmetric positive-definite matrices,” *J. Matrix Analysis Applications*, vol. 29, no. 1, pp. 328–347, 2007.
- [28] K. Kronander and A. Billard, “Learning compliant manipulation

- through kinesthetic and tactile human-robot interaction,” *IEEE transactions on haptics*, vol. 7, no. 3, pp. 367–380, 2013.
- [29] F. J. Abu-Dakka, L. Rozo, and D. G. Caldwell, “Force-based learning of variable impedance skills for robotic manipulation,” in *2018 IEEE-RAS 18th International Conference on Humanoid Robots (Humanoids)*. IEEE, 2018, pp. 1–9.
- [30] O. Siméoni, H. V. Vo, M. Seitzer, F. Baldassarre, M. Oquab, C. Jose, V. Khalidov, M. Szafraniec, S. Yi, M. Ramamonjisoa *et al.*, “Dinov3,” *arXiv preprint arXiv:2508.10104*, 2025.
- [31] D. Rakita, B. Mutlu, and M. Gleicher, “Relaxedik: Real-time synthesis of accurate and feasible robot arm motion.” in *Robotics: Science and Systems*, vol. 14. Pittsburgh, PA, 2018, pp. 26–30.
- [32] Y. Wang, P. Praveena, D. Rakita, and M. Gleicher, “Rangedik: An optimization-based robot motion generation method for ranged-goal tasks,” in *2023 IEEE Int. Conf. on Robotics and Automation (ICRA)*. IEEE, 2023, pp. 9700–9706.
- [33] Y. Zhu, A. Joshi, P. Stone, and Y. Zhu, “Viola: Imitation learning for vision-based manipulation with object proposal priors,” *arXiv preprint arXiv:2210.11339*, 2022.
- [34] Epic Games, “Unreal engine,” <https://www.unrealengine.com/>, accessed: 2025-12-28.
- [35] Y. Chang, P. Y. Chen, Z. Wang, M. M. Chiamonte, K. Carlberg, and E. Grinspun, “Licrom: Linear-subspace continuous reduced order modeling with neural fields,” in *SIGGRAPH Asia 2023 Conference Papers*, 2023, pp. 1–12.
- [36] Z. Zong, X. Li, M. Li, M. M. Chiamonte, W. Matusik, E. Grinspun, K. Carlberg, C. Jiang, and P. Y. Chen, “Neural stress fields for reduced-order elastoplasticity and fracture,” in *SIGGRAPH Asia 2023 Conference Papers*, 2023, pp. 1–11.
- [37] C. Romero, D. Casas, M. Chiamonte, and M. A. Otaduy, “Learning contact deformations with general collider descriptors,” in *SIGGRAPH Asia 2023 Conference Papers*, 2023, pp. 1–10.
- [38] Y. Wang, C. Sifferman, and M. Gleicher, “Exploiting task tolerances in mimicry-based telemanipulation,” in *2023 IEEE/RSJ Int. Conf. Intelligent Robots Systems (IROS)*. IEEE, 2023, pp. 7012–7019.
- [39] Y. Wang, P. Praveena, and M. Gleicher, “A design space of control coordinate systems in telemanipulation,” *IEEE Access*, vol. 12, pp. 64 150–64 164, 2024.
- [40] S. G. Hart and L. E. Staveland, “Development of nasa-tlx (task load index): Results of empirical and theoretical research,” in *Advances in psychology*. Elsevier, 1988, vol. 52, pp. 139–183.